CHEMISTRY OF MATERIALS

ARTICLE

pubs.acs.org/cm

Development of Direct Cell Inorganic Barrier Film Technology Providing Exceptional Device Stability for CIGS Solar Cells

Paul R. Elowe,*,† Matthew A. Stempki,§ Steve J. Rozeveld,⊥ and Marty W. DeGroot*,‡

§Dow Solar Solutions and ⊥Dow Analytical Sciences, The Dow Chemical Company, Midland, Michigan 48667, United States

Supporting Information

ABSTRACT: Failure analysis of solar cells and model substrates coated with silicon nitride barrier thin films has led to important conclusions regarding the major factors leading to barrier degradation. Data gathered from optical densitometry, microscopy (optical, SEM, and TEM), as well as infrared spectroscopy, have revealed that nitride film delamination, because of poor adhesion to silver collection grids, and nitride oxidation, facilitated by sodium migration, were the leading causes of barrier failure. Based on this study, a new method for barrier deposition utilizing an ultrathin tantalum nitride adhesion layer was implemented. Copper indium gallium diselenide ($CuIn_{1-x}Ga_xSe_2$, denoted hereafter as CIGS) solar cells treated with a TaN_x/SiN_x thin film bilayer architecture have shown exceptional stability under accelerated damp heat conditions. Devices treated with these coatings have retained >90% of initial photovoltaic performance for an average of >1900 h at 85 °C/85% RH, with several devices showing damp heat survival for >3000 h.

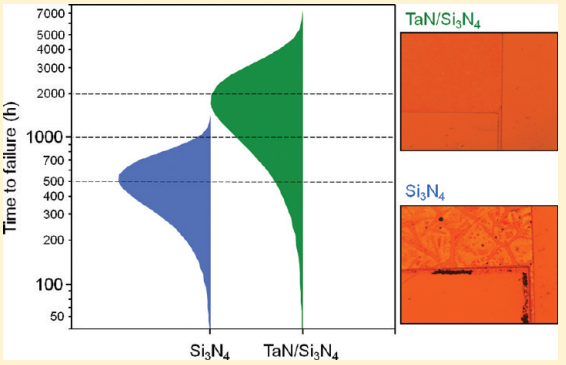

KEYWORDS: CIGS, moisture barrier, thin film, damp heat, solar cell

INTRODUCTION

With champion cell efficiencies of >19%[1] and demonstrated module capabilities of >14% efficiency,[2] photovoltaic modules based on copper indium gallium diselenide ($CuIn_{1-x}Ga_xSe_2$, denoted hereafter as CIGS) are among the leading technology options for high-efficiency, low-cost terrestrial applications. In parallel, with continuous efforts focused on narrowing the gap between laboratory- and production-scale power density, significant attention has been directed toward development of robust encapsulation technologies to ensure stable performance over the requisite lifetime of commercial modules. Indeed, CIGS devices are vulnerable to a variety of moisture-induced degradation pathways,[3] with the *i*-ZnO and CdS layers being particularly susceptible.[4] Encapsulation of modules under glass has proven to be an efficient method to prevent moisture ingress;[5] however, the addition of a glass encapsulation to the packaging leads to inevitable loss of flexibility in the module, which is a highly desirable feature in the BIPV industry.

With varying degrees of success, organic and inorganic thin films, as well as hybrids thereof, have been investigated as potential flexible moisture barriers.[6] We were interested in the development of direct cell inorganic coating technologies as an approach to impart improved solar cell stability as one component in a simplified encapsulation package. Silicon nitride (SiN_x) films are attractive candidates, because of their chemical stability, high density, and transparency in the visible region. Protection of an organic light-emitting diode (LED) for >1000 h under accelerated exposure conditions using SiO_xN_y/SiN_x stacked films prepared by catalytic chemical vapor deposition (CVD) was recently demonstrated.[7] Glick and co-workers have investigated the use of silicon oxynitride barriers for CIGS PV packaging; however, the results indicated that these films did not offer sufficient protection.[8] Studies in our laboratories have shown that CIGS solar cells coated with either SiN_x or SiO_xN_y/SiN_x stacked films exhibited extended durability, compared to similar samples lacking a protective coating. Understanding the root causes of failure of these inorganic barriers is a crucial path toward the development of improved direct cell coatings. Herein, we summarize findings of an extensive failure analysis and present a new approach to overcome predominant barrier degradation pathways. The resulting devices exhibit exceptional stability under damp heat conditions.

EXPERIMENTAL SECTION

Several different sample types were prepared in this study. Aluminum-coated glass samples were used as model substrates for moisture ingress evaluation, using optical densitometry and microscopy. Similar model substrates were prepared with a glass/Al/ITO/Ag grid structure. Si(100) wafers were used as substrates for characterization of inorganic thin barrier films by Fourier transfer infrared (FTIR) spectroscopy. Glass substrates were cleaned via a standard protocol consisting of sequential

Received: May 5, 2011
Revised: July 25, 2011
Published: August 05, 2011

ultrasonication in 2% Novaclean solution, isopropanol, and Nanopure water, with rinsing between each step, followed by drying in an oven (110 °C). Double-sided polished boron-doped Si(100) wafers (50 mm diameter, 0.45−0.50 mm thickness, ρ = 1−20 Ω cm) were purchased from Silicon Valley Microelectronics. Samples of aluminum-coated soda−lime or borosilicate glass were prepared by DC magnetron sputtering (200 W) of a 150-mm Al target (99.999%, Process Materials Inc.) in an argon atmosphere (4.5 mTorr) for 2 min.

Thin Film Deposition. Deposition of metal nitride thin films was carried out by radio frequency (RF) magnetron reactive sputtering of metal targets in an Ar/N_2 atmosphere, using an Anatech Hummer sputter system with a 300 W, 13.56 MHz RF power supply and a 50-mm planar magnetron sputter source. The chamber possesses sputter-down configuration and a rotary substrate platen. The chamber was evacuated to a routinely achieved base pressure of $<9 \times 10^{-6}$ Torr over a period of 2−3 h. Circular targets (50 mm diameter, 6.4 mm thickness) of *p*-doped Si (99.999%) Ta (99.99%) and Ti (99.99%) were provided by Process Materials, Inc. Indium tin oxide (ITO) films were prepared using a custom RF magnetron sputter chamber from a 100-mm-diameter, 5-mm-thick ITO ceramic target (90 wt % In_2O_3, 10 wt % SnO_2) using gas flows of argon (14 sccm) and oxygen (2 sccm), controlled using mass flow controllers, to achieve a working gas pressure of 2.8 mTorr. The substrate temperature was held at 150 °C during deposition. A mask was applied to shield an area of the sample and expose only the area to be covered by a conductive grid. Layers of nickel and then silver having a total thickness of ∼1600 nm were sequentially deposited by E-beam evaporation. Prior to evaporation, the chamber base pressure is reduced to $<2 \times 10^{-6}$ Torr. All depositions were carried out at 9.0 kV, with current values of 0.130 and 0.042 A for Ni and Ag, respectively. The deposition rates were monitored using a Maxtek 260 quartz crystal deposition controller at 2.0 Å/s and 15.0 Å/s for Ni and Ag, respectively. Ni shots (99.9999%), obtained from International Advanced Materials, were evaporated from a 7 cm^3 graphite crucible, while Ag pellets (99.9999%, Alfa Aesar) were evaporated from a 7 cm^3 molybdenum crucible.

CIGS Cell Fabrication. CIGS photovoltaic devices were prepared on 2-in.-square soda-lime glass substrates, 0.7 mm thick. A layer of molybdenum was sputter-deposited at 200 W, 6×10^{-3} mbar on the glass substrate, to a final thickness of ∼750−800 nm. CIGS absorber layer was deposited by a multistage metal coevaporation process based on a three-stage process reported by NREL.[9] A cadmium sulfide buffer layer was deposited by chemical bath deposition (CBD) by dipping samples into a mixture of 33 mL of 0.015 M $CdSO_{4(aq)}$ and 42 mL 14.5 M $NH_4OH_{(aq)}$ (concentrated NH_3) at 70 °C. After 1 min, 33 mL of 0.75 mL thiourea was added and the reaction was allowed to proceed for 7 min. Samples were dried at 110 °C for 30 min, then heated to 200 °C. The window layer, *i*-ZnO, was prepared by RF magnetron sputtering of a ZnO target at 60 W and 10 mTorr sputtering pressure (0.15% O_2 in argon sputtering gas) to a final thickness of ∼70 nm. The devices were completed by deposition of ITO and Ni/Ag collection grids under the conditions described above. The cells were then treated with SiN_x or TaN_x/SiN_x according to the procedures described above.

Characterization. A Nicolet 710 FTIR spectrometer was used for IR spectral analysis of silicon nitride films on Si(100) substrates. All spectra were collected in the absorbance mode in the wavenumber range between 4000 cm^{-1} and 450 cm^{-1}. A total of 128 scans were averaged for each spectrum (∼2-min acquisition time) with 4 cm^{-1} resolution and Happ−Genzel apodization. Because of the highly reflective surfaces of the silicon wafers and the thin inorganic films deposited onto the wafers, fringes (the wavelength-dependent periodic absorbance fluctuation pattern) were observed for almost every spectrum. This issue could potentially be mitigated by tilting the sample surface so that the IR beam forms an incident angle close to the Brewster's angle, or by mathematical treatment of the digital spectra.[10] We found this to be unnecessary, because the absorbance modulation caused by the fringe pattern was rather weak in the wavenumber range that we were interested in (between 1300 cm^{-1} and 700 cm^{-1}), compared to the actual absorbance of the deposited film.

Optical density measurements were carried out using an X-Rite 361T transmission densitometer using a 3-mm aperture. Density measurements were taken for both orthogonal and ultraviolet responses. The former was used for comparison of relative moisture barrier performance.

Optical microscopy images were collected on a Leitz Aristomet optical microscope with Paxit! imaging system software. All images were recorded at 5× and 10× magnifications. The samples for SEM analysis were prepared by mounting the samples onto aluminum SEM stubs. The samples were coated with ∼5 nm of conductive osmium coating prior to SEM-EDS mapping, to eliminate charging effects. The samples were then coated with a 20-nm-thick layer of conductive chromium coating prior to FIB analysis. SEM imaging and EDS (energy-dispersive X-ray analysis) were done using the FEI Nova 600 SEM system. TEM and EDS data were collected using a JEOL Model 2010F field-emission gun (FEG) transmission electron microscopy (TEM) system that was equipped with a Bruker AXS XFlash 4030 energy-dispersive X-ray spectrometry (EDS) detector with an energy resolution of 137 eV/channel (SN 1576). The TEM was operated at an accelerating voltage of 200 keV. Conventional TEM images were recorded using a Gatan multiscan digital camera (Model Ultrascan 1000) with a CCD size of 2048 pixels × 2048 pixels. Time-of-flight secondary ion mass spectrometry (ToF-SIMS) was performed on an Ion-ToF IV instrument. For depth profile sputtering, a Cs^+ ion source was used at an energy of 3 keV and a primary ion current of 26 nA. A Bi_3^+ cluster ion source was used for analysis; analyses were performed in bunched mode at 25 keV energy with a primary ion current of ∼0.05 pA. An area of 250 μm^2 was selected for the depth profile Cs^+ ion crater, and, within this, a 100-μm^2 area was probed for analysis using the Bi_3^+ ion beam. Cs^+ sputtering occurred for 15 s between each analysis cycle, for a total of 406 cycles in all. Analysis of collected data was performed using Ionspec 4.0 Service Pack 11 and Ionspec Print Wizard 4.1.0.0.

The device efficiency is extracted from a current−voltage ($I-V$) characteristic curve that is measured before and after each step using a Class AAA solar simulator. The $I-V$ characteristic measurement apparatus and procedure meet the requirements specified in the IEC 60904 (parts 1−10) and 60891 standards. For each $I-V$ measurement, electrical contact is established using a 5-μm-radius tungsten probe tip placed in contact with the collection grid bus bar and the molybdenum-coated back side was grounded through a gold-coated brass platen. During the $I-V$ measurement, the temperature of the platen and the device is maintained at 25 °C. Prior to the measurement, the xenon arc lamp is permitted 15 min to stabilize. The lamp irradiance then is set to AM1.5 1000 W/m^2, using a calibrated silicon reference device with a BK-7 filter. The relative uncertainty in the efficiency

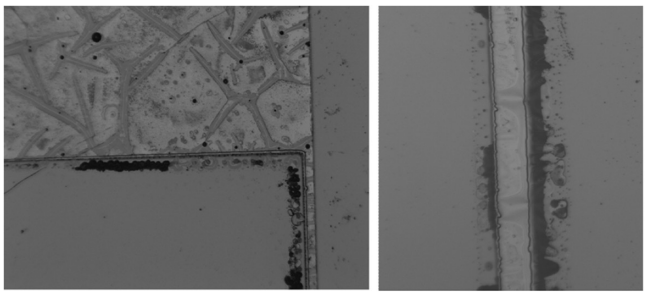

Figure 1. Optical microscopy images showing oxidation of the aluminum film (observed as dark areas) near the silver grids. The image on the left also shows evidence of cracking of the barrier layer.

measurement is ±4%. JMP statistical software version 8.02 was used for survival modeling.

RESULTS AND DISCUSSION

Screening evaluation of the moisture barrier performance of thin-film candidates has been carried out by monitoring the change in optical density of aluminum-coated substrates during exposure to aggressive damp heat conditions (115 °C/100% relative humidity (RH)). Water vapor transmission is monitored by optical changes due to oxidation of the aluminum film, in a similar fashion as the so-called calcium (Ca) test.[11] This approach enables a high-throughput comparison and failure analysis of barrier films without tedious preparation and packaging procedures required for Ca. Recently, it was demonstrated that moisture ingress through an inorganic barrier film at 115 °C/100% RH is accelerated by more than a facor of 8 in this environment, versus standard 85 °C/85% RH conditions.[12] In addition to providing a semiquantitative assessment of moisture barrier performance, this approach provides an opportunity for qualitative identification of key defects enabling moisture ingress for a given inorganic barrier film. [While the relative degradation due to moisture ingress can be quantified for comparison of respective barrier film candidates, the use of this approach has not been certified for the calculation of actual WVTR data.] Assessment of potential degradation modes for silicon nitride-coated solar cells was further extended to model substrates that were comprised of a thin aluminum film on soda−lime glass (SLG), a sputtered indium tin oxide (ITO) layer, and nickel−silver collection grids (deposited by evaporation). A silicon nitride layer (150 nm) was then deposited on the substrate via reactive sputtering. Samples were exposed to accelerated damp heat conditions (115 °C/100% RH) in a pressure vessel, and optical density and optical microscopy data were collected at various intervals. Microscopy images reveal that significant oxidation of the aluminum layer occurs near the silver grid lines (evident as black areas, which are due to the formation of optically transparent aluminum oxide), after only 47 h of damp heat exposure (see Figure 1). Also evident is the incidence of defects on the top surface of the grids. On the other hand, minimal damage is observed over the majority of the ITO/SiN_x interface, as demonstrated by optical density measurements and microscopic analysis. Further analysis by top-down SEM confirms the occurrence of major degradation to the silicon nitride layer over and around the grid locations after damp heat exposure for 380 h (see Figure 2). The degradation occurs in the form of ruptures and fissures created in the silicon nitride layer resulting from delamination

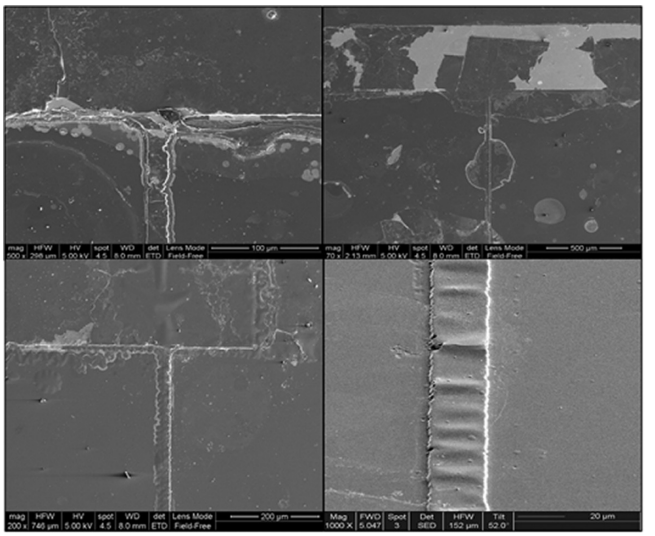

Figure 2. Top-down SEM images showing damage to the silicon nitride layer in the vicinity of the silver grids, following damp heat exposure for 380 h at 115 °C/100% relative humidity (RH).

during accelerated exposure. The effect is so severe in certain areas that sections of silicon nitride are completely eradicated from the surface of the silver grid. The buckling observed in the silicon nitride layer (see Figure 2) is indicative of failures due to residual compressive stress in the silicon nitride film at the Ag interface.[13] The high residual compressive stress is a function of both the coefficient of thermal expansion (CTE) mismatch between the Ag (18 ppm/°C) and Si_3N_4 (3 ppm/°C), and the high deposition rate that is typical of sputtering processes.[14] The buckling due to compressive stress can lead to the formation of open voids or channels that enable moisture ingress to the Si_3N_4/Ag interface that further decreases adhesion at the interface and provides further susceptibility to cracks and delamination. These defects were not observed outside of the grid region, indicating that similar disruption of the ITO/SiN_x interface does not occur during damp heat exposure, perhaps due to lower CTE mismatch.[15] FIB-SEM analysis of a cross section of a silver grid line in a region with apparent rupturing of the silicon nitride layer further depicts delamination of the nitride film from silver, where a gap forms between the two layers (see Figure 3). The delamination of silicon nitride in this manner is consistent with the observation of higher shear stress located at the corners of silicon nitride-passivated aluminum and copper interconnect lines in silicon integrated circuits.[16]

Further evaluation of the barrier film failure that was conducted using top-down elemental (EDS) mapping of glass/Al/ITO/Si_3N_4 model substrates revealed significant oxidation of the Si_3N_4 film, particularly near the grid regions, following accelerated damp heat exposure. Figure 4 shows nitrogen and oxygen contents of an area in the vicinity of the grid. The darker regions from the nitrogen map suggest extensive loss of nitrogen, particularly emphasized over the thin gridline. However, this oxidation is not exclusive to the grid regions, as evidenced by TEM/EDS analysis showing clear oxidation of the nitride layer in regions away from the grid. It is obvious from these images that oxidation proceeds from the top layer down (see Figure 5). Oxidation of the surface of the Si_3N_4 films during damp heat exposure was also confirmed by FTIR spectroscopy, which showed a shift of the primary resonance by ~60 cm^{-1} to higher

dx.doi.org/10.1021/cm201281v |*Chem. Mater.* 2011, 23, 3915–3920

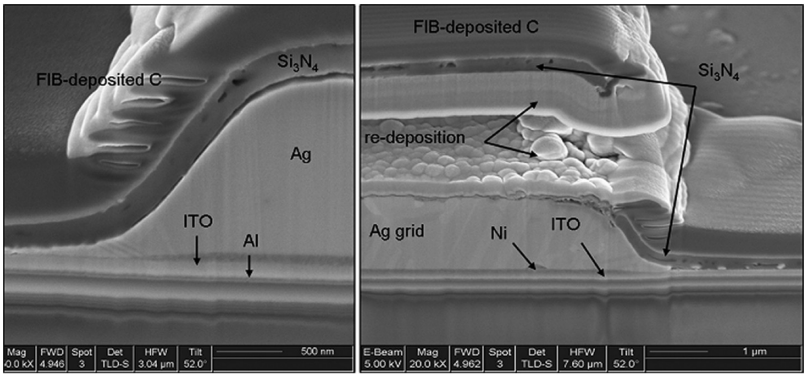

Figure 3. Cross-section SEM images showing delamination and rupturing of the silicon nitride layer from a silver grid, following damp heat exposure for 380 h at 115 °C/100% RH.

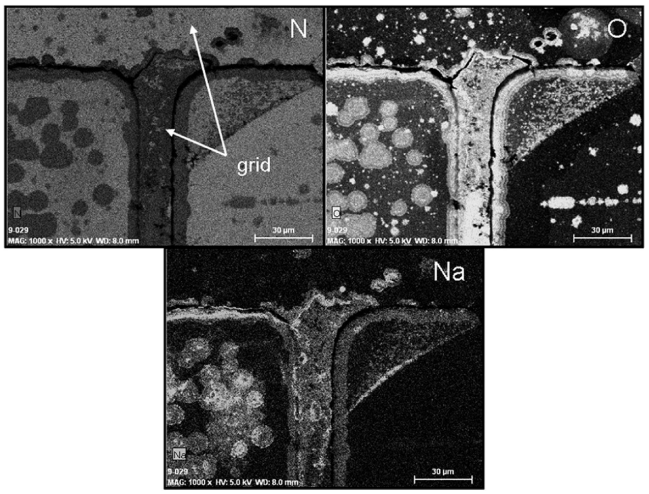

Figure 4. Elemental maps (EDS) for N (top, left), O (top, right), and Na (bottom) in a grid region, following damp heat exposure for 380 h at 115 °C/100% RH.

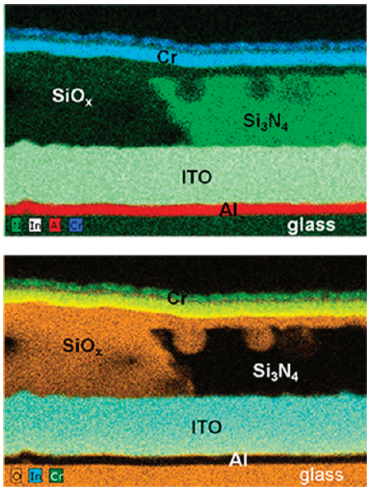

Figure 5. TEM/EDS cross sections of a glass/Al/ITO/Si_3N_4 model substrate outside of the grid regions after 380 h at 115 °C/100% RH. Top: nitrogen (green), indium (white), aluminum (red), chromium (blue). Bottom: oxygen (orange), indium (blue), chromium (green).

energy, consistent with increased oxygen content in the film (see the Supporting Information). It has been shown previously that SiO_xN_y barrier films, by themselves, do not perform as well as the nitride analogs,[17] presumably because of the lower density of SiO_xN_y films. Nonetheless, despite significant oxidation of the silicon nitride layer during damp heat exposure, the SiO_xN_y or SiO_x (and the subsequent ITO layer) continues to fulfill the function to prevent moisture ingress, as evidenced by the lack of oxidation of the Al layer in these locations. Notably, aluminum-coated glass samples with ITO and no barrier layer showed substantial oxidation of the layer after only 20 h of aggressive damp heat exposure. This further indicates that the delamination of the Si_3N_4 barrier from the grid is the major driver for moisture ingress.

Referring again to Figure 4, the map also reveals the presence of significant quantities of Na with a distribution that indicates an intimate relationship between oxidation and sodium migration to the top layers in the grid regions. The results of EDS mapping suggest that sodium species, such as sodium hydroxide (NaOH) and sodium oxide (Na_2O), from the glass substrate may accelerate oxidation of SiN_x (for example, as the Si_3N_4 species). It has been shown that Na_2O can dissolve silicon dioxide (SiO_2) to generate a liquid sodium silicate ($Na_2O \cdot xSiO_2$) film, for which there are rapid diffusion rates for O_2 inward and, after oxidation of Si_3N_4, N_2 outward (eqs 1 and 2).[18] While there is currently no indication that sodium directly affects the integrity of the Si_3N_4/Ag (indeed, model samples prepared on borosilicate glass substrates show cracking and delamination of the nitride layer, albeit to a lesser extent qualitatively), it may function to accelerate Si_3N_4 oxidation and further degradation in regions where cracking and delamination of the barrier layer occur.

$$Na_2O(s) + xSiO_2(s) \rightarrow Na_2O \cdot xSiO_2(l) \quad (1)$$

$$Si_3N_4(s) + 3O_2(g) \rightarrow 3SiO_2(s) + 2N_2(g) \quad (2)$$

The results described above demonstrate that the efficacy of silicon nitride coatings for the protection of CIGS solar cells is limited by the poor Si_3N_4/Ag grid interface, because of low interfacial adhesion or interfacial stress. This poses a significant threat to the integrity of the device, because it leads to rupturing of the protective layer and provides propitious sites for significant moisture ingress. The delamination of the silicon nitride layer also provides channels to facilitate sodium migration to the surface of the device, the presence of which appears to facilitate further degradation of the silicon nitride layer. Since sodium is a

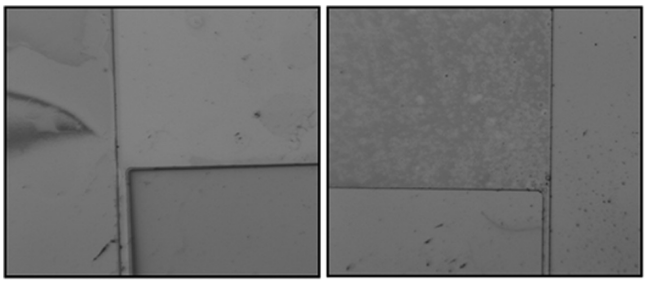

Figure 6. Typical optical microscope images of grid regions for model substrates coated with TiN_x/SiN_x (left) and TaN_x/SiN_x (right), following damp heat exposure (115 °C/100% RH) for 210 h.

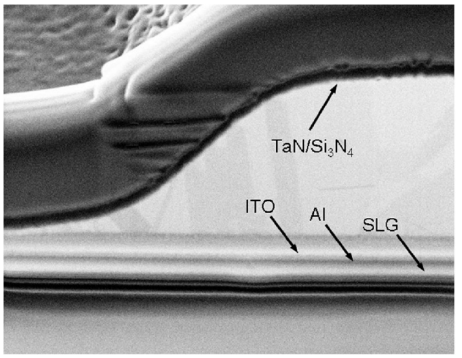

Figure 7. Cross-section SEM image of grid regions for model substrates coated with TaN_x/SiN_x following damp heat exposure (115 °C/100% RH) for >420 h.

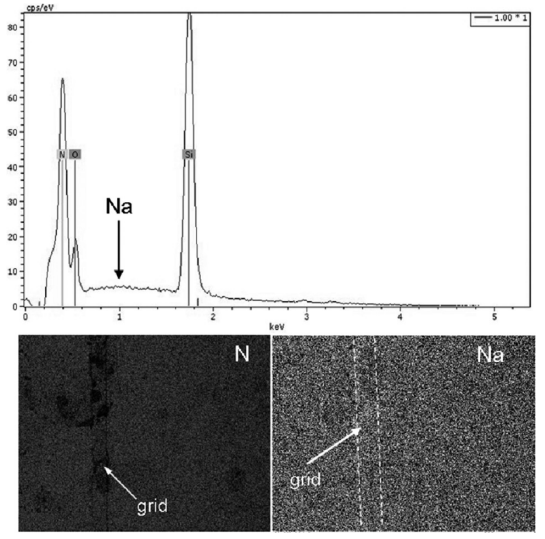

Figure 8. SEM−EDS results showing the absence of oxidation and Na migration to the surface near the grid regions for model substrates coated with TaN_x/SiN_x, following damp heat exposure (115 °C/100% RH) for >420 h.

desirable component of CIGS solar cell devices,[19] SiN_x degradation facilitated by the presence of sodium remains relevant even when nonglass substrates, such as stainless steel, are employed.

Based on the above-mentioned results, it was postulated that the deficiencies could be overcome via the incorporation of a thin film that could provide improved interfacial integrity and

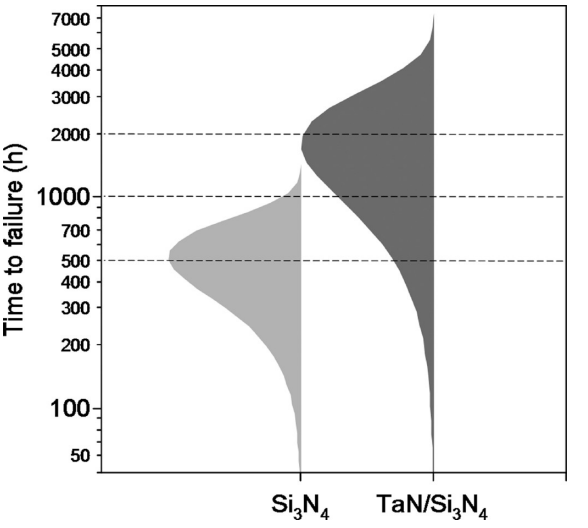

Figure 9. Weibull distribution curves for failure data for CIGS solar cells coated with SiN_x (150 nm) or TaN_x/SiN_x (10/140 nm), following damp heat exposure (85 °C/85% RH).

mitigation of Na diffusion. Titanium and tantalum nitride have been used as diffusion barriers in microelectronics applications.[20] In a similar fashion as described above, model substrates were prepared on Al-coated SLG substrates, except that an ultrathin layer (10 nm) of TaN_x or TiN_x was deposited between the ITO/grid and the SiN_x interface. A comparison of optical microscopy images of the $TiN_x(TaN_x)/SiN_x$-coated samples following damp heat exposure with those of samples coated only with SiN_x (see Figure 1) reveals marked improvement in the integrity of the silicon nitride layer (see Figure 6). The TiN_x and TaN_x interfacial layer indeed mitigates delamination of the SiN_x film, which is a leading cause of further cracking of the layer. After 210 h at 115 °C/100% RH, the Ni/Ag grid lines remain sharp with no sign of aluminum oxidation in the vicinity. As discussed above, oxidation of the aluminum film is already at an advanced stage for SiN_x-coated samples after only 47 h under the same conditions.

Further investigation of the TaN_x/SiN_x-coated samples included cross-section analysis via FIB-SEM. A sample exposed to >420 h at 115 °C/100% RH showed no delamination of the barrier layer from the silver grid (see Figure 7). This result further provides compelling evidence of the beneficial role of tantalum or titanium nitride thin films in improving barrier film/collection grid interface. In addition, EDS mapping of the sample surface after >420 h reveals no detection of sodium content, even on top and around the silver grids, which was established as a predominant area of sodium migration (see Figure 8). As a consequence, and further supporting the hypothesis that nitride oxidation was further facilitated by the presence of sodium species, EDS maps show virtually no oxidation of the silicon nitride layer and no loss in nitrogen content. The presence of a few localized oxygen-rich areas is attributed to surface impurities deposited onto the surface of the sample during accelerated exposure.

Following the improvements observed via the incorporation of an ultrathin TiN_x or TaN_x barrier layer on model substrates, TaN_x (10 nm)/SiN_x (140 nm) multilayer films were sequentially deposited on CIGS devices prepared on glass substrates. CIGS devices were also treated with SiN_x (150 nm) for comparison. The devices were introduced to damp heat conditions of 85 °C/85% RH and the performance of the devices was monitored via

dx.doi.org/10.1021/cm201281v |*Chem. Mater.* 2011, 23, 3915–3920

$I-V$ characterization at intervals over an extended time frame. Cells were considered to have failed at the time at which the normalized efficiency decreased below 90% of the initial cell value. Since the cells were tested at various intervals during damp heat exposure, interval censoring was utilized in order to obtain nonparametric estimates of the survival function. Figure 9 shows time-to-failure Weibull distribution curves for CIGS devices coated with SiN_x or TaN_x/SiN_x. The presence of the ultrathin TaN_x barrier layer has an incredible effect on the survival probability of the CIGS devices. A parametric survival fit reveals a statistically significant influence of material type on the probability of failure. Characteristic life estimates (Weibull α parameter) of 1970 h at 85 °C/85% RH were calculated for the TaN_x/SiN_x-coated cells versus 530 h for cells coated with 150-nm SiN_x films. Fitted Weibull survival estimates reveal >70% survival probability for 1000 h under damp heat conditions for TaN_x/SiN_x-coated CIGS cells. Remarkably, several devices have exhibited >90% efficiency retention following damp heat exposure for >3000 h. To the knowledge of the authors, the observed performance is unprecedented for CIGS solar cells in the absence of an encapsulation package and offers new opportunities for development of fully flexible CIGS solar modules using a simplified encapsulation technology.

CONCLUSIONS

We have described the results of a detailed failure analysis study of barrier coated CIGS solar cells and model substrates. Accelerated damp heat exposure results in significant delamination and cracking of silicon nitride barrier layers in the region of the silver collection grids. Further evidence reveals that barrier degradation is facilitated by sodium migration. Treatment of CIGS solar cells with an ultrathin tantalum nitride adhesion layer prior to the silicon nitride layer results in a remarkable improvement in stability of CIGS devices under accelerated damp heat conditions. Devices treated with these coatings have retained >90% of initial photovoltaic performance for an average of >1900 h at 85 °C/85% RH, with several devices showing damp heat survival for >3000 h.

ASSOCIATED CONTENT

Supporting Information. This material is available free of charge via the Internet at http://pubs.acs.org.

AUTHOR INFORMATION

Corresponding Author

*E-mail: prelowe@dow.com (P.R.E.), wdegroot2@dow.com (M.W.D.).

Present Addresses

[†]677 Building, Michigan Operations, The Dow Chemical Company, Midland, MI 48674. Ph: (+1)989-636-5033. E-mail: prelowe@dow.com.

[‡]Dow Electronic Materials, 451 Bellevue Rd. Newark, DE 19709. Ph: (+1)302-366-0500, ext. 6330. E-mail: wdegroot2@dow.com.

ACKNOWLEDGMENT

The authors are grateful to the following colleagues for valuable discussions: Rebekah Feist, Ryan Gaston, Marc Langlois and Mike Mills. Jeff D'Archangel, Jeff Mitchell, Charlie Wood, Shawn Chen, and Brandon Kern are thanked for analytical support.

REFERENCES

(1) (a) Jackson, P.; Hariskos, D.; Lotter, E.; Paetel, S.; Wuerz, R.; Menner, R.; Wischmann, W.; Powalla, M. *Prog. Photovolt. Res. Appl.* **2011**, DOI:10.1002/pip.1078. (URI: http://onlinelibrary.wiley.com/doi/10.1002/pip.1078/full, accessed June 3, 2011.) (b) Ramanathan, K.; Contreras, M. A.; Perkins, C. L.; Asher, S.; Hasoon, F. S.; Keane, J.; Young, D.; Romero, M.; Metzger, W.; Noufi, R.; Ward, J.; Duda, A. *Prog. Photovolt. Res. Appl.* **2003**, *11*, 225.

(2) *Green Energy News* **2010**, *15* (24) (URI: http://www.green-energy-news.com/nwslnks/clips910/sep10005.html, accessed June 3, 2011.)

(3) (a) Deibel, C.; Dyakonov, V.; Parisi, J.; Palm, J.; Zweigart, S.; Karg, F. *Thin Solid Films* **2002**, *403−404*, 352. (b) Schmidt, M.; Braunger, D.; Schaffler, R.; Schock, H. W.; Rau, U. *Thin Solid Films* **2000**, *283*, 361–362. (c) Heske, C.; Richter, G.; Chen, Z.; Fink, R.; Umbach, E.; Riedl, W.; Karg, F. *J. Appl. Phys.* **1997**, *82*, 2411.

(4) (a) Wennerberg, J.; Kessler, J.; Bodegard, M.; Stolt, L. In *Proceedings of the 2nd World Conference on Photovoltaic Energy Conversion*, 1998; p 116. (b) Pern, F. J.; To, B.; DeHart, C.; Li, X.; Glick, S. H.; Noufi, R. Technical Report No. NREL/CP-520-42792, National Renewable Energy Laboratory, Golden, CO, 2008.

(5) Powalla, M.; Dimmler, B. *Thin Solid Films* **2000**, *361−362*, 540.

(6) (a) Olsen, L. C.; Gross, M. E.; Kundu, S. N.; Shafarman, W. N. *Proc. 26th IEEE Photovolt. Spec. Conf.* **1997**, 1. (b) Olsen, L. C.; Gross, M. E.; Graff, G. L.; Kundu, S. N.; Xi, C.; Lin, S. *Proc. SPIE* **2008**, *7048*, 1. (c) Herz, K.; Kessler, F.; Wächter, R.; Powalla, M.; Schneider, J.; Schulz, A.; Schumacher, U. *Thin Solid Films* **2002**, *403−404*, 384.

(7) Ogawa, Y.; Ohdaira, K.; Oyaidu, T.; Matsumara, H. *Thin Solid Films* **2008**, *516*, 611.

(8) Glick, S. H.; del Cueto, J. A.; Terwilliger, K. M.; Jorgensen, G. J.; Pankow, J. W.; Keyes, B. M.; Gedvilas, L. M.; Pern, F. J. Technical Report No. NREL/CP-520-38959, National Renewable Energy Laboratory, Golden, CO, 2005.

(9) Repins, I.; Contreras, M. A.; Egaas, B.; DeHart, C.; Scharf, J.; Perkins, C. L.; To, B.; Noufi, R. *Prog. Photovolt. Res. Appl.* **2008**, *13*, 209.

(10) Pistorius, A. M. A.; DeGrip, W. J. *Vib. Spectrosc.* **2004**, *36*, 89.

(11) Chen, T.-S.; Wuu, D.-S.; Chiang, C.-C.; Chen, Y.-P.; Horng, R.-H. *Plasma Proc. Polym.* **2007**, *4*, 180.

(12) DeGroot, M. W.; Elowe, P. R.; Wilbur, J.; George, J.; Feist, R. K. *Proc. 34th IEEE Photovolt. Spec. Conf.* **2009**, 450.

(13) Abdallah, A. A.; Bouten, P. C. P.; den Toonder, J. M. J.; de With, G. *Thin Solid Films* **2008**, *516*, 1063.

(14) Wu, P.-H.; Lin, I.-K.; Yan, H.-Y.; Ou, K.-S.; Chen, K.-S.; Zhang, X. *Sens. Actuators A* **2011**, *168*, 117.

(15) Neerinck, G.; Vink, T. J. *Thin Solid Films* **1996**, *278*, 12.

(16) He, D.; Zhang, C.; Chiang, D.; Zheng, T.; Lucero, A.; Stage, R.; Atluri, V. *Proc. 55th Electron. Compon. Technol. Conf.* **2005**, 349.

(17) Iwamori, S.; Gotoh, Y.; Moorthi, K. *Vacuum* **2003**, *68*, 113.

(18) Fox, D. S.; Jacobsen, N. S. *J. Am. Ceram. Soc.* **1988**, *71*, 128.

(19) (a) Rudmann, D.; Brémaud, D.; da Cunha, A. F.; Bilger, G.; Strohm, A.; Kaelin, M.; Zogg, H.; Tiwari, A. N. *Thin Solid Films* **2005**, *480−481*, 55. (b) Rudmann, D.; da Cunha, A. F.; Kaelin, M.; Zogg, H.; Tiwari, A. N. *Mater. Res. Soc. Symp. Proc.* **2003**, *763*, 53. (c) Rudmann, D.; da Cunha, A. F.; Kaelin, M.; Kurdesau, F.; Zogg, H.; Tiwari, A. N.; Bilger, G. *Appl. Phys. Lett.* **2004**, *84*, 1129.

(20) (a) Gillan, E. G.; Kaner, R. B. *Inorg. Chem.* **1994**, *33*, 5693. (b) Ostling, M.; Nygren, S.; Petersson, C. S.; Norstrom, H.; Buchta, R.; Blom, H. O.; Berg, S. *Thin Solid Films* **1986**, *145*, 81. (c) Aryasomayajula, A.; Valleti, K.; Aryasomayajula, S.; Bhat, D. G. *Surf. Coat. Technol.* **2006**, *201*, 4401.